ISPRS Journal of Photogrammetry and Remote Sensing 106 (2015) 1–15

Contents lists available at ScienceDirect

ISPRS Journal of Photogrammetry and Remote Sensing

journal homepage: www.elsevier.com/locate/isprsjprs

Sparse-based reconstruction of missing information in remote sensing images from spectral/temporal complementary information

Xinghua Li [a], Huanfeng Shen [a,b,*], Liangpei Zhang [b,c], Huifang Li [a]

[a] School of Resource and Environmental Sciences, Wuhan University, Wuhan, Hubei Province, China
[b] Collaborative Innovation Center for Geospatial Information Technology, Wuhan University, Wuhan, Hubei Province, China
[c] The State Key Laboratory of Information Engineering in Surveying, Mapping, and Remote Sensing, Wuhan University, Wuhan, Hubei Province, China

ARTICLE INFO

Article history:
Received 22 October 2014
Received in revised form 30 January 2015
Accepted 17 March 2015

Keywords:
Analysis model
Missing information (MI)
Remote sensing (RS)
Sparse representation
Spectral and temporal information
Synthesis model

ABSTRACT

Because of sensor failure and poor observation conditions, remote sensing (RS) images are easily subjected to information loss, which hinders our effective analysis of the earth. As a result, it is of great importance to reconstruct the missing information (MI) of RS images. Recent studies have demonstrated that sparse representation based methods are suitable to fill large-area MI. Therefore, in this paper, we investigate the MI reconstruction of RS images in the framework of sparse representation. Overall, in terms of recovering the MI, this paper makes three major contributions: (1) we propose an analysis model for reconstructing the MI in RS images; (2) we propose to utilize both the spectral and temporal information; and (3) on this basis, we make a detailed comparison of the two kinds of sparse representation models (synthesis model and analysis model). In addition, experiments were conducted to compare the sparse representation methods with the other state-of-the-art methods.

1. Introduction

Due to the sensors being out of working order (e.g., Aqua Moderate Resolution Imaging Spectroradiometer (MODIS) band 6 (Li et al., 2014), the Landsat ETM+ SLC-off problem (Zeng et al., 2013), the row anomaly problem of Aura OMI (Yan et al., 2012)) or in a cloudy atmosphere, the involved regions in remote sensing (RS) images often have invalid information, which we call missing information (MI). It is noteworthy that only passive RS images (visible and infrared) are affected by the atmosphere. MI greatly reduces the availability of RS images. Thus, reconstruction of the MI of RS images is a hot topic in the RS field. It is in fact similar to the old and well-known inpainting (Bertalmio et al., 2000) problem in the image processing field. To date, a number of methods have been aimed at image inpainting, e.g., interpolation (Kokaram et al., 1995), partial differential equations (PDE) (Bertalmio, 2006), total variation (TV) (Chan et al., 2005), and the Huber–Markov method (Shen and Zhang, 2009). For small and sparse missing areas of RS images, these methods can obtain a satisfactory recovery effect. However, they are not able to reconstruct large missing areas. These methods are all based on spatial complementation. Unfortunately, the MI area is usually large in RS images. As a result, the spatial complementation based methods cannot successfully reconstruct the MI of RS images.

For multispectral RS images, the bands are correlated with each other in the spectral domain, and it is the band-to-band correlation which we call spectral complementation. Generally speaking, the spectral complementation plays an important role on the condition that (for multispectral images) some bands have MI and others are intact. The authors in Li et al. (2014), Wang et al. (2006), Rakwatin et al. (2009), Shen et al. (2011), and Gladkova et al. (2012) made the best use of spectral complementation to reconstruct the corrupted band by modeling the spectral relationship between the corrupted band and the other good bands (one or more). As a result of the effective mathematical or physical restrictions, they reduced the error of the polynomial fitting. Cheng et al. (2014) proposed a variation-based method by combining the strengths of a TV method and a nonlocal method. Although this method aims to reconstruct a multispectral image in which all the spectral bands have the same MI, it is still suitable for the case stated here. Additionally, Shen et al. (2014) proposed a sparse representation based method which adaptively weights the intact bands

* Corresponding author at: School of Resource and Environmental Sciences, Wuhan University, Wuhan, Hubei Province, China.
E-mail address: shenhf@whu.edu.cn (H. Shen).

http://dx.doi.org/10.1016/j.isprsjprs.2015.03.009
0924-2716/

according to the spectral importance. In short, the spectral complementation based methods have an advantage over the spatial complementation based methods when coping with large-area MI. However, if the atmosphere is cloudy and rainy, the RS images acquired in the visible and infrared ranges will be occluded by clouds. In this case, the spectral complementation is ineffective.

Correspondingly, a number of scholars have resorted to other sources of complementary information. For RS images (over the same region) acquired from different periods, they are correlated in the temporal domain, and it is the image-to-image correlation which we call temporal complementation. Hereafter, the images from different periods and over the same region are referred to as "multitemporal images". Temporal interpolation (Inglada and Garrigues, 2010) and filters (Jakubauskas et al., 2001; Chen et al., 2004; Roerink et al., 2000) are the most basic reconstruction methods; however, in order to obtain a satisfactory reconstruction, they are dependent on a long time series of data. Regression analysis (Zeng et al., 2015), mosaicing or completion (Helmer and Ruefenacht, 2005; Lin et al., 2014; Cheng et al., 2014), and geostatistical methods (Zhang et al., 2009) are simple and common algorithms which just use a reference image from another period; however, they sometimes do not obtain a good effect in the junction of a missing region and good region. Recently, sparse representation based methods (Li et al., 2014; Lorenzi et al., 2013) have also been used in this field and have obtained promising results. Unfortunately, the temporal complementation based methods have a fatal flaw in that once the multitemporal images show a significant land-cover change, the methods are no longer applicable.

In recent years, researchers have verified that the sparse representation based methods are appropriate for recovering large-area MI (Guillemot and Le Meur, 2014), which has inspired our interest. Firstly, we make a simple review of sparse representation, as follows.

- **Sparse representation.** Sparse representation was first proposed in the 1980s (von zur Gathen and Kaltofen, 1985; Coppersmith and Davenport, 1985; Pissanetzky, 1984), and is a representation that accounts for most or all the information of a signal by a linear combination of only a small number of elementary signals, called atoms (Gemmeke et al., 2011). In the 1990s, Mallat and Zhang (1993) proposed the concept of the overcomplete dictionary to initiate a new development stage. Sparse representation has found applications in numerous domains and tasks, such as image inpainting, denoising, super-resolution, fusion, classification, and target detection. According to the crude estimation of the ISI Web of Science, there have been more than 4000 papers related to sparse representation (Nam et al., 2013). To the best of our knowledge, Olshausen and Field (1996) first introduced sparse representation into the field of natural image processing, and since then it has developed into two main classes: synthesis models and analysis models.
- **Synthesis models.** As the name implies, synthesis models synthesize a signal $x \in \mathbb{R}^m$ by the multiplication of two components, i.e., $x = D\alpha$, where $D \in \mathbb{R}^{m\times n}(m < n)$ is an overcomplete dictionary (i.e. D is a matrix with m rows and n columns) and $\alpha \in \mathbb{R}^n$ is the representation coefficient. The columns of D are called dictionary atoms. This expression is called a sparse representation, on the condition that the vector α is sparse, i.e., $\|\alpha\|_0 = k \ll n$, meaning that the number of nonzero elements (k) is far less than the total number (n). In other words, the signal x can be represented as a sparse linear combination of the k atoms from the redundant dictionary (Aharon et al., 2006; Elad and Aharon, 2006). The last decade has witnessed a great amount of investigation into synthesis models, which attempt to obtain a better sparse approximation to the real signal. To date, synthesis models have been successfully applied to image denoising (Elad and Aharon, 2006), super-resolution (Rehman et al., 2012; Jianchao et al., 2010), inpainting (Mairal et al., 2008; Fadili et al., 2009), and deblurring (Weisheng et al., 2011). Relatively speaking, they are a mature class of model with solid theoretical foundations and extensive applications.
- **Analysis models.** These models take an analysis point of view (Rubinstein et al., 2013). Differing from the synthesis models, which decompose the signal to get a redundant dictionary and sparse coefficients, analysis models aim to gain a sparse outcome by multiplying the signal by an analysis operator (dictionary). Given an analysis dictionary $\Omega \in \mathbb{R}^{p\times m}(p > m)$, (i.e. Ω is a matrix with p rows and m columns), the analyzed outcome is $y = \Omega x \in \mathbb{R}^p$. The representation y should be sparse (or we say "cosparse"), meaning $\|y\|_0 = p - l \ll p$ (l denotes the number of zeros in y). These zeros carve out the low-dimensional subspace that the signal belongs to Rubinstein et al. (2013). Analysis models have been preliminarily and empirically applied to the restoration of information, including signal and digital image recovery (denoising) (Yaghoobi et al., 2013; Ophir et al., 2011; Yaghoobi et al., 2012; Giryes et al., 2011), and the MI recovery of natural images (Hawe et al., 2013). To the best of our knowledge, analysis models have not yet been used in the processing of RS images. Compared to the synthesis models, they are a young class of model.

Among the methods above, the authors of Shen et al. (2014), Li et al. (2014), and Lorenzi et al. (2013) adopted sparse representation based methods, but not analysis-based methods. In this paper, we propose an analysis-based method. We also want to know, between the synthesis and analysis models, which is the better approach to reconstruct missing RS information? In addition, is it better to extract the complementary information from both the spectral and temporal domains? We attempt to answer these questions in this paper.

This paper makes three contributions to the reconstruction of missing RS information: (1) we introduce an analysis model to reconstruct the MI in RS images; (2) a detailed comparison is made between the synthesis and analysis models; and (3) the spectral and temporal complementary information is jointly used.

The rest of this paper is organized as follows. In Section 2, we present the algorithms used for reconstructing the MI of RS images, based on synthesis and analysis models, respectively. Section 3 provides the specific comparisons between the two models, using only multispectral images, using only multitemporal images, and using both multispectral and multitemporal images. Finally, the conclusions are drawn in Section 4.

2. Algorithms

As stated previously, the sparse representation based methods are suitable for the reconstruction of large-area MI. To date, a number of researchers have proposed sparse-based reconstruction methods for RS images (using synthesis models) (Shen et al., 2014; Li et al., 2014; Lorenzi et al., 2013). However, to the best of our knowledge, analysis models aimed at recovering the MI of RS images have not been investigated. Accordingly, we propose an analysis model based algorithm in this paper. For RS images, the spectral and temporal complementation lays a solid foundation for the reconstruction of the MI. However, the present methods use only one kind of complementation to reconstruct the MI of RS images. Our other goal is to explore whether the two

approaches can be simultaneously used. Overall, the proposed algorithm makes the best use of the sparse property and complementation for reconstructing the missing RS information. In the following algorithms, multispectral and multitemporal images can be jointly used. Therefore, before the algorithms are introduced, we cover how to organize multisource RS images.

2.1. How to organize multispectral/temporal RS images

In our framework, the experimental RS images can be multispectral, multitemporal, or a combination. As a result, we need to organize the images from the different sources. The basic idea is to superimpose them onto a three-dimensional (3D) data cube. Without loss of any generality, we suppose that all the RS images are multispectral. In other words, each image among the multitemporal images is multispectral. The 3D cube (jointly using the multispectral and multitemporal images) is derived as in the following steps: Suppose that one band (we call it the corrupted band) of the multispectral image (we call it the corrupted image) has MI. All the bands of the corrupted image and the same band (that is the corrupted band) extracted from other multitemporal images are superimposed onto the 3D cube. In fact, the cube consists of multisource bands. If we only use the spectral complementation, the cube will be the same as the corrupted image; and if we only use the temporal complementation, the cube will be completely extracted from the same band of the different multitemporal images. Fig. 1 shows the superimposed result of the data cube. As can be seen, the cube has multiple layers, in which each layer represents a single-channel item from the "spectral channel" and the "temporal channel". "Spectral channel" means the bands from the corrupted image itself. "Temporal channel" means the bands extracted from other multitemporal images. For example, if the image has five bands, and we have four images in all, the 3D cube with spectral and temporal complementation will have eight bands (five bands are from the corrupted image, and three bands are from other images); the 3D cube with spectral complementation will have five bands (all are from the corrupted image); and the 3D cube with temporal complementation will have four bands (all are from different images). We then reorder the layers, and this process is described in Section 2.2.

2.2. Strategies for reducing image differences

As is widely known, for multispectral and multitemporal RS images, their component bands have clear radiance differences, which is also reflected in the data cube (as derived in Section 2.1). As shown in Fig. 2(b) and (e), if the kind of difference is paid no attention to, it will pass into the final reconstruction results. Thus, it is necessary to eliminate these differences. In our opinion, we think that the corrupted band and the good bands have a transformation relationship. Depending on this reasonable transformation, the intrinsic differences can be effectively relieved. To date, there have been different kinds of transformation methods, which can be linear or nonlinear. For simplicity, we selected the general linear transformation in the experiments: least-squares fitting (Rakwatin et al., 2009).

Let the 3D cube be $\{x_i\}_{i=1}^{N} \in \mathbb{R}^{h\times w}$, and x_i denotes the ith layer of the cube. For convenience, we suppose that x_1 is the corrupted band, and $\{x_i\}_{i=2}^{N}$ $(N \geqslant 2)$ are the good bands. As shown in Fig. 3, Ψ denotes the missing area in x_1 and the same area in x_i, and Ψ^- denotes the complementary region for the corresponding Ψ. Based on the intact areas of x_1 and x_i, we obtain the transformation relationship. We first assume they satisfy the expression:

$$x_1(\Psi^-) = a_i x_i(\Psi^-) + b_i, \quad i = 2,3,\ldots,N \tag{1}$$

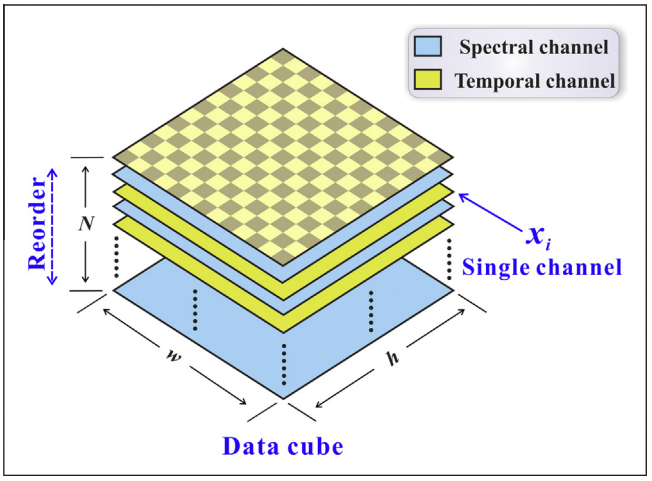

Fig. 1. Sketch diagram of the superimposition of multispectral/temporal RS images.

where $x_1(\Psi^-)$ indicates the elements contained in the region Ψ^- of x_1, as does $x_i(\Psi^-)$. a_i and b_i are the coefficients acquired by the least-squares fitting method, as follows:

$$a_i = \frac{u\sum x_1(\Psi^-)x_i(\Psi^-) - \sum x_1(\Psi^-)\sum x_i(\Psi^-)}{u\sum (x_i(\Psi^-))^2 - (\sum x_i(\Psi^-))^2}, \quad i = 2,3,\ldots,N \tag{2}$$

$$b_i = \frac{\sum x_1(\Psi^-) - a_i\sum x_i(\Psi^-)}{u}, \quad i = 2,3,\ldots,N \tag{3}$$

where u denotes the pixel number of $x_1(\Psi^-)$. Once the coefficients are known, the linear transformation is realized as:

$$x_i^{new}(\Psi^- \cup \Psi) = a_i x_i(\Psi^- \cup \Psi) + b_i, \quad i = 2,3,\ldots,N \tag{4}$$

where x_i^{new} denotes the transformed x_i.

Usually, in the framework of patch-based sparse representation, the natural overlapping order of the multiple layers in the 3D cube does not guarantee the optimal path. Ram et al. (2013) proposed a shortest spatial path ordering of the image patches. Inspired by this, we seek a reasonable temporal/spectral path which reorders the multisource bands to make better use of their complementary correlations. The basic idea is to ensure that the bands with stronger correlations are closer together in a patch. As stated in our previous paper (Li et al., 2014), the optimized path is similar to fused lasso (Tibshirani et al., 2005; Rinaldo, 2009), which is designed for problems with features that can be ordered in some meaningful way. To date, there have been many different kinds of metrics of correlation proposed, and in our framework, the metric of correlation is picked as the correlation coefficients (CCs) between the intact regions (Ψ^-) of the corrupted and good bands. Suppose CC_i is the CC between $x_1(\Psi^-)$ and $x_i(\Psi^-)$, then it is calculated by:

$$CC_i = \frac{\sum_{\Psi^-}\left(x_1(\Psi^-) - \mu_{x_1(\Psi^-)}\right)\left(x_i(\Psi^-) - \mu_{x_i(\Psi^-)}\right)}{\left(\sum_{\Psi^-}(x_1(\Psi^-) - \mu_{x_1(\Psi^-)})^2\right)^{\frac{1}{2}}\left(\sum_{\Omega}(x_i(\Psi^-) - \mu_{x_i(\Psi^-)})^2\right)^{\frac{1}{2}}}, \quad i = 1,2,\ldots,N \tag{5}$$

where $\mu_{x_1(\Psi^-)}$ and $\mu_{x_i(\Psi^-)}$ represent the average values of $x_1(\Psi^-)$ and $x_i(\Psi^-)$, respectively. It can be easily seen that $CC_1 = 1$ is the maximum. Once the CCs are calculated, the permutation order inside the patch is determined, which is sorted from the highest CC to the lowest. The reordering permutation is the optimized path of our patch-based reconstruction method. For a convenient description, LTRP refers to "linear transformation and reordering permutation" in the following.

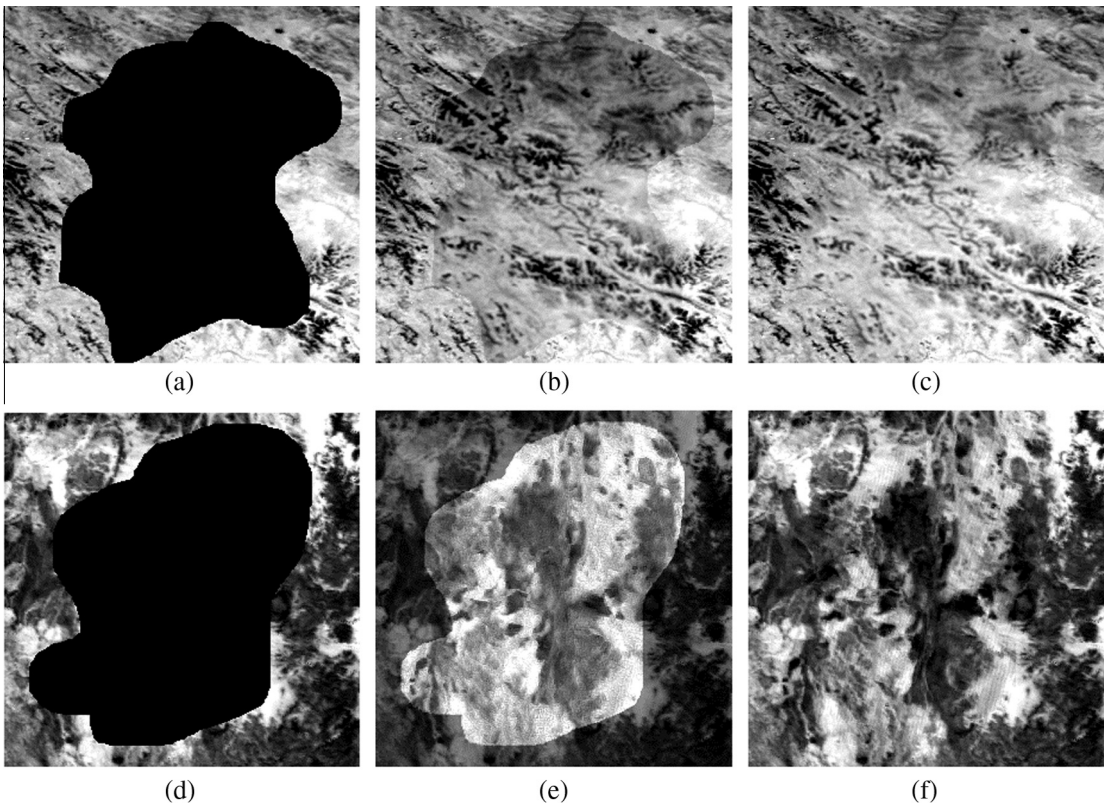

Fig. 2. The reconstruction results using multispectral and multitemporal images, respectively, based on a sparse model. (a) The corrupted band 1. (b) Directly reconstructed result of band 1 using the multispectral image. (c) The corresponding result of band 1 after reducing the differences. (d) The corrupted band 2. (e) Directly reconstructed result of band 2 using the multitemporal images. (f) The corresponding result of band 2 after reducing the differences.

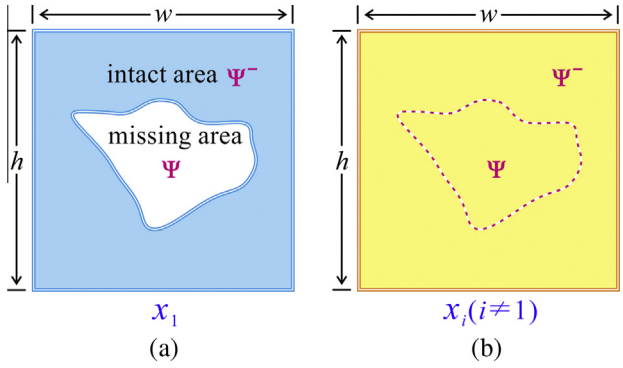

Fig. 3. Schematic diagram of corrupted and good bands of an RS image. (a) A corrupted band. (b) A good band.

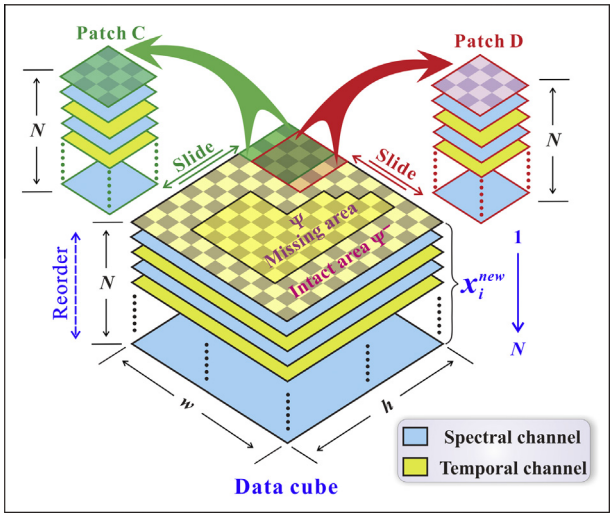

Fig. 4. Sketch diagram of the procedure for extracting patches.

2.3. Procedure of extracting patches

Based on the previous sections, the single-channel x_1 and $\{x_i^{new}\}_{i=2}^{N}$ consist of a 3D data cube. For the convenience of description, let $x_1^{new} = x_1$. As with the popular methods based on the sparse representation model (Aharon et al., 2006; Elad and Aharon, 2006; Mairal et al., 2008), the first thing that needs doing is to extract the patches. Fig. 4 shows the procedure of extracting patches. In this cube, we extract the sliding patches with the size of $B \times B \times N$ pixels (e.g., in Fig. 4, N represents the layer of Patch C, and B is the number of columns/rows of Patch C), as many as possible, starting from the top-left-most patch, e.g., Patch C and Patch D in Fig. 4. Therefore, with $x_i^{new} \in \mathbb{R}^{h \times w}$ we finally have q $[q = (w - B + 1) \times (h - B + 1)]$ patches. The patches are then ordered lexicographically as column-stacked vectors to form a two-dimensional (2D) $X \in \mathbb{R}^{NB^2 \times q}$.

2.4. Synthesis model for reconstructing the MI

Based on $X \in \mathbb{R}^{NB^2 \times q}$, as obtained in Section 2.3, we utilize the synthesis model to reconstruct the MI. The observation model is as follows:

$$X = M \odot (D\alpha) + \varepsilon_1 \tag{6}$$

where $M \in \mathbb{R}^{NB^2 \times q}$ denotes a mask with zeros and ones implying where the information is lost, $D \in \mathbb{R}^{NB^2 \times n}$ (n is the atom number with $NB^2 < n$) represents the redundant dictionary, $\alpha \in \mathbb{R}^{n \times q}$ is the corresponding sparse representation, ε_1 is the observation error, and $E(\odot)F$ denotes the point-wise (element-wise) product of E and F.

As a result, in the synthesis model, the objective function for reconstructing the MI from the corrupted image is presented as:

$$\arg\min_{D,\alpha} \lambda \|X - M \odot (D\alpha)\|_2^2 + \|\alpha\|_0 \tag{7}$$

where λ denotes the regularization parameter. We use the same method (K-SVD dictionary learning) as described in Elad and Aharon (2006) and Elad (2010) to solve α and update D. The basic idea is to solve α and D alternately. Firstly, assuming that D is known (i.e., the initial is given), α is solved by (8) as follows:

$$\widehat{\alpha} = \arg\min_{\alpha} \|\alpha\|_0 \ s.t. \ \|X - M \odot (D\alpha)\|_2^2 \leqslant cn\sigma^2 \tag{8}$$

where c is a constant satisfying the situation that it is larger than the largest eigenvalue of DD^T (D^T is the transpose of D), n counts the existing pixels in the observed data, σ^2 denotes the variance of the noise (supposing that the data are degraded by zero-mean Gaussian noise). This process is also called sparse coding. In fact, the sparse coefficients α are solved column by column. Once all the columns of α are obtained, we can then fix them and turn to updating D as (9):

$$\widehat{D} = \arg\min_{D} \|X - M \odot (D\alpha)\|_2^2 \tag{9}$$

The second process is usually called dictionary learning. For more details, we recommend the reader refer to Elad and Aharon (2006) and Elad (2010). In general, multiple alternations between α and D are required, which lays a foundation for a more accurate recovery result. Once the representation α is obtained under the current dictionary D, the MI of X is reconstructed according to (10).

$$\widehat{X} = \widehat{D}\widehat{\alpha} \tag{10}$$

where $\widehat{X}$ means the reconstructed version of X. An inverse operation of the patch extraction in Section 2.3 is then immediately imposed on $\widehat{X}$ to obtain the final recovered image.

2.5. Analysis model for reconstructing the MI

In this section, we introduce the analysis model for reconstructing the MI. For $X \in \mathbb{R}^{NB^2 \times q}$, as obtained in Section 2.3, the observation model of cosparse representation (with analysis models, researchers usually refer to "cosparse") is:

$$Y = \Omega(M \odot X) + \varepsilon_2 \tag{11}$$

where $\Omega \in \mathbb{R}^{p \times NB^2}$ (p is the atom number with $p > NB^2$) denotes the analysis dictionary, M and $(\odot)$ have the same meanings as in (6), $Y \in \mathbb{R}^{p \times q}$ denotes the cosparse coefficients, and ε_2 represents the error.

Before the formal introduction to the analysis model for the reconstruction of MI in RS images, we describe some of the basic concepts of an analysis model. In an analysis model, it should lay an emphasis on the zeros of the outcome. For (11), we define $\Omega_\Lambda(M \odot X) = 0$, where Ω_Λ is a sub-matrix of Ω that contains only the rows indexed in Λ, and Λ is called the co-support of X (Rubinstein et al., 2013). Correspondingly, the co-rank for the given analysis dictionary Ω is defined by the rank of Ω_Λ. In fact, the co-support determines the orthogonal subspace of the original X. If r denotes the dimension of the subspace that X belongs to, the co-rank is $NB^2 - r$. Consequently, in an analysis model, the objective function is of the form:

$$\arg\min_{Z,\Lambda} \|M \odot Z - X\|_2^2 \ s.t. \ \Omega_\Lambda X = 0 \quad Rank(\Omega_\Lambda) = NB^2 - r \tag{12}$$

where Z is the ideal value of X, r represents the dimension of the subspace that X belongs to. We use a similar method to that described in Rubinstein et al. (2013) to solve Z and Λ. As in the synthesis model, the analysis model resorts to a two-stage optimization scheme. In the first stage, we calculate Z with the analysis dictionary Ω fixed. In the second stage, we update Ω with the calculated Z from the first stage. The two-stage optimization scheme is repeated alternately until the predefined number is reached. Firstly, supposing that the initial Ω is given, the backward-greedy pursuit method in Rubinstein et al. (2013) is used for solving Z, and the basic expression is as (13). It is noteworthy that Z is still solved column by column, as in the synthesis model.

$$\widehat{Z} = (I - \Omega_\Lambda^\dagger \Omega_\Lambda)X \tag{13}$$

where I represents an identity matrix, and $\Omega_\Lambda^\dagger$ denotes the pseudo-inverse of Ω_Λ.

Once all the columns of $\widehat{Z}$ are calculated in the first stage, we turn to updating the analysis dictionary Ω. The approximate solution of (14) is used for calculating the co-support of Ω and updating Ω. In Rubinstein et al. (2013), Rubinstein et al. indicated that this problem is equivalent to finding the smallest singular value by singular value decomposition (SVD), and we refer the reader to this reference for further details.

$$\widehat{\Lambda} = \arg\min_{\Lambda} \|\Omega_\Lambda(M \odot Z)\|_2^2 \tag{14}$$

In the second stage, the process of calculating Λ amounts to the updating of Ω. After adequate alternation between Z and Ω, the optimal reconstruction of the MI can be obtained by the expression of (13). When the ideal 2D value of X is solved, the columns will be transformed into the previous patches, as in Section 2.3. All the patches will then return to their original positions and make up the original 3D data cube. In fact, the transformation is the inverse process of extracting patches. Since neighboring patches are partly overlapped, one pixel may be included in different patches. In other words, one pixel may be reconstructed many times, according to how many patches it belongs to. Thus, the result is the average of the multiple reconstructions.

In fact, the sparse representation methods (synthesis model and analysis model) are powerless in some cases: (1) spatial failure; if only the spatial complementation is available, when the missing area is very large, the sparse representation methods cannot recover the MI effectively with insufficient supplementary information; (2) spectral failure; if the atmosphere is cloudy and rainy, many of the spectral bands of a multispectral image will be covered by thick clouds, and the sparse representation methods cannot obtain a satisfactory effect only using the corrupted image itself; (3) temporal failure; all the temporal complementation methods are sensitive to abrupt land-cover changes. In consideration of the limitations of the sparse representation methods in the three kinds of complementation, we propose the integrated utilization of them to fully utilize their individual advantages.

3. Comparisons and experiments

We conducted experiments to reconstruct the MI of RS images using the most basic synthesis and analysis models described in Section 2. In an actual situation, when the atmosphere is cloudy or rainy, only the temporal complementation is helpful. However,

if the time interval is so long that the land cover shows obvious changes, this is not the case anymore. When the sky is clear, the spectral complementation and temporal complementation are both useful. In order to find the best complementation method, the following three classes of experiments were undertaken: (1) based on the spectral complementation only (using a multispectral image); (2) based on the temporal complementation only (using multitemporal images); (3) jointly based on the spectral and temporal complementation (using both a multispectral image and multitemporal images). When multitemporal images were used, the time interval was not long. Note that when affected by a cloudy and rainy atmosphere, both the spectral and temporal complementary information may be unavailable. Therefore, to make sure that the spectral and temporal complementary information were both available, we only undertook simulated experiments. In addition, we also made a comparison between the sparse representation methods and the state-of-the-art methods for a sequence of RS images (multispectral and multitemporal).

The experimental images were the 500-m resolution L1B reflectance product of MODIS onboard the Aqua and Terra satellites, which were directly downloaded from the NASA website (http://ladsweb.nascom.nasa.gov/data/search.html). This product has seven bands in all. Table 1 shows the original data, in which the prefix "MOD" denotes Terra MODIS, and "MYD" denotes Aqua MODIS. To acquire multitemporal images over the same geographic area, these reflectance products were georeferenced by the MODIS conversion toolkit (MCTK), which was downloaded from the NSDIC website (http://nsidc.org/data/modis/tools.html). The experimental platform was a PC with an Intel 3.4 GHz CPU and 8 GB of memory. In the experiments, without any special instructions, $B = 2, n = 256, D \in \mathbb{R}^{4N\times 256}$ (N is the layer number of the cube), $p = 256, \Omega \in \mathbb{R}^{256\times 4N}$, and $r = 2$. Note that the initials of D and Ω were both discrete cosine transform (DCT) bases.

In the experiments, we used mean absolute error (MAE), mean squared error (MSE), mean relative error (MRE), and CC [calculated by (5)] as the evaluation indicators. Given $c \in \mathbb{R}^K$ and $d \in \mathbb{R}^K$ (for brevity, we supposed that they were both vectors here) as the data to be compared, then MAE is defined by the following expression:

$$\mathrm{MAE}(c,d) = \frac{1}{K}\sum_{i=1}^{K}|c_i - d_i| \tag{15}$$

MSE is calculated by:

$$\mathrm{MSE}(c,d) = \frac{1}{K}\sum_{i=1}^{K}(c_i - d_i)^2 \tag{16}$$

Suppose d is the reference data, then MRE is computed by:

$$\mathrm{MRE}(c,d) = \frac{1}{K}\sum_{i=1}^{K}\frac{|c_i - d_i|}{d_i} \tag{17}$$

Table 1
Experimental data.

No.	Data name
1	MOD02HKM.A2013306.0735.005.2013309010548
2	MOD02HKM.A2013307.0815.005.2013309013119
3	MYD02HKM.A2013308.1030.005.2013309160325
4	MOD02HKM.A2013309.0805.005.2013309160525
5	MOD02HKM.A2013311.0750.005.2013311200217
6	MYD02HKM.A2013312.1005.005.2013313180516
7	MOD02HKM.A2013313.0740.005.2013313140307
8	MYD02HKM.A2013315.1035.005.2013316184251

3.1. MI reconstruction using only a multispectral image

This section focuses on the ability of the synthesis and analysis models to reconstruct the lost RS information by extracting spectral complementary information. Two experiments were undertaken. Each experiment used only one multispectral image. The two images were cropped from different regions of the data ordered No. 4 in Table 1, with the size of $300 \times 300 \times 7$. For simplicity, they were called Image A and Image B, respectively. In the experiments, the original bands were artificially corrupted. The original bands are shown in Fig. 5(a). With 47.7867% and 48.6633% of pixels lost, respectively, the corrupted bands are shown in Fig. 5(b). The missing pixels were then reconstructed by the synthesis and analysis methods with LTRP.

Fig. 5 shows the corrupted bands of Image A and Image B before and after the missing pixel reconstruction, respectively, based on the synthesis and analysis models. From the overall visual perspective, the results of the two models both have a satisfactory effect and do not show a great difference. For a more detailed comparison, we zoom in on the green box areas in Fig. 5. Through careful observation, it can be found that the original images have some outliers (noisy points), which are removed in the results of the analysis model. In other words, the analysis model has a denoising effect. On the other hand, compared to the original images, the reconstruction results of the analysis model have stronger structures relative to those of the synthesis model. To some extent, the synthesis model results in edge expansion [e.g., the blue circled areas in Fig. 5(c)]. In short, the analysis model does better in denoising and structure enhancement than the synthesis model, according to the reconstruction of the MI in a multispectral image.

In order to further expose the qualitative differences of the reconstructions of the synthesis and analysis models in Fig. 5, we resorted to scatter plots between the originals and reconstructions. As shown in Fig. 6, the points in the scatter plot of the analysis model [Fig. 6(b) and (d)] are distributed more closely around the red diagonal than those of the synthesis model [Fig. 6(a) and (c)]. As pointed out in Elad et al. (2007), the analysis model reconstructs the data through various forward measurements, while the synthesis model seeks the reconstruction as a combination of atoms. Since there are accurate prior measurements, the analysis model is more successful in reconstructing the MI than the synthesis model, and the points on the scatter plot are closer to the diagonal. The scatter plots strongly indicate that the analysis model outperforms the synthesis model, as with the visual effect.

After the previous qualitative assessments, the objective evaluations follow. Table 2 shows the quantitative evaluations by the metrics of MAE, MSE, MRE, CC, and time cost for the results in Fig. 5 (in this table, the rows with sources labeled S are the objective evaluations for this multispectral experiment). Generally speaking, the lower the values of MAE, MSE, MRE, and time cost, the better the result; and the higher the value of CC, the better the result. As shown in Table 2 (rows labeled "S"), as far as time cost is concerned, the analysis model has an overwhelming advantage over the synthesis model. As noted by Rubinstein et al. (2013), one advantage of the analysis model is that it disjoints the update of the atoms of the analysis dictionary, enabling all the atoms to be updated in parallel, as opposed to the synthesis model, which updates the dictionary atoms one after another, resulting in a high time cost. As a result, the analysis model performs more efficiently. Furthermore, in terms of other quantitative indicators, for both the synthesis model and analysis model, the results show a clear improvement. However, the improvement of the analysis model is more obvious than that of the synthesis model. The reason for this is that the analysis model is restricted by the forward measurement of the intact components of the image itself, and the synthesis model is restricted by the combination of a group of atoms,

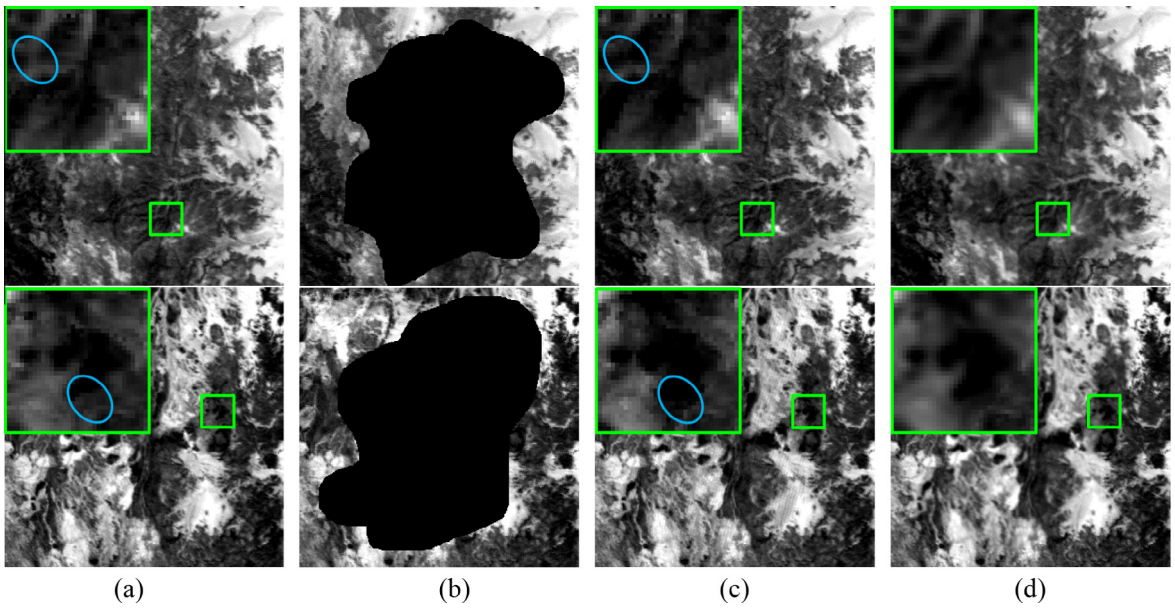

Fig. 5. The reconstruction results of the corrupted bands in Image A and Image B, based on the synthesis and analysis models, using a multispectral image. The upper row is for Image A, and the lower row is for Image B. (a) The original image. (b) The corrupted image. (c) Reconstruction of the synthesis model with LTRP. (d) Reconstruction of the analysis model with LTRP.

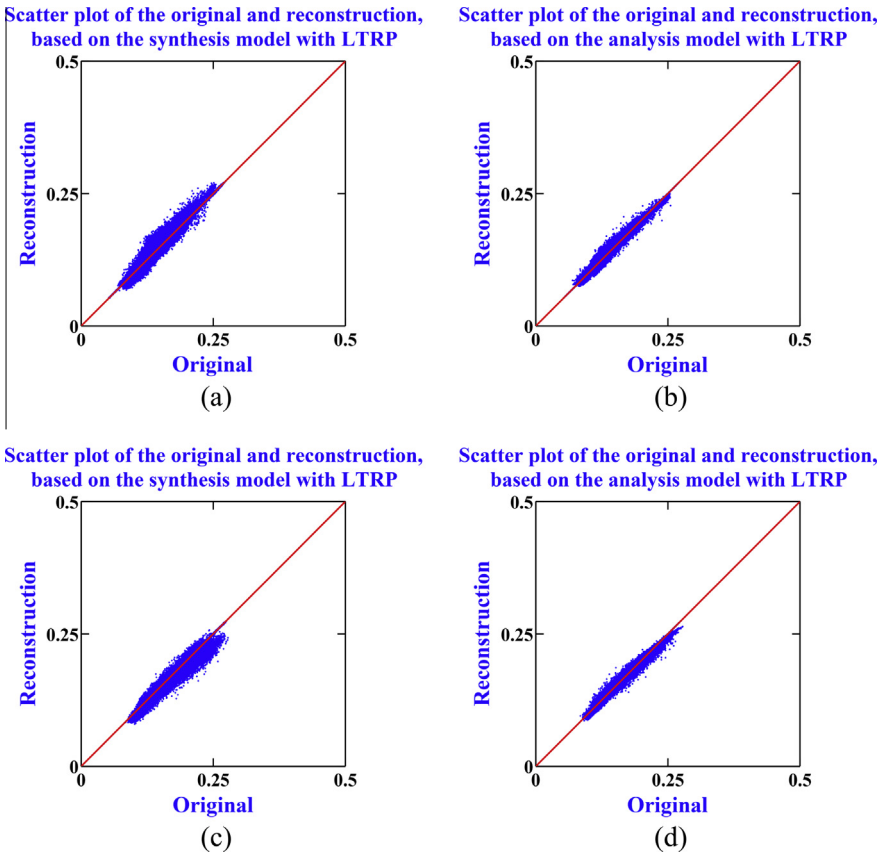

Fig. 6. The scatter plots between the originals and the reconstructions of the synthesis and analysis models in Fig. 5(c)–(d), respectively. (a) For upper Fig. 5(c), synthesis model. (b) For upper Fig. 5(d), analysis model. (c) For lower Fig. 5(c), synthesis model. (d) For lower Fig. 5(d), analysis model.

and the latter approach results in more errors. Overall, Table 2 (rows labeled "S") indicates that the analysis model is a more promising approach than the synthesis model.

To achieve an in-depth comparison of the abilities of the synthesis and analysis models to utilize spectral complementary information, experiments to reconstruct the lost information with different numbers of extra spectral bands were also carried out. For Image A and Image B, they have seven spectral bands, which lays the foundation for our experiments. The corrupted bands were both the first channels of the corresponding corrupted images.

Table 2
Comparison of the reconstructions of the synthesis and analysis models by extracting information from different sources.

Original data	Methods	Sources	MAE/10^{-3}	MSE/10^{-5}	MRE/%	CC	Time/min
Upper Fig. 5(a)	Corrupted	\	66.9471	895.6120	52.2133	0.6579	\[d]
	Synthesis	S[a]	3.5181	4.1120	2.7268	0.9898	7.1590
		T[b]	3.5851	3.9120	2.8329	0.9898	7.4570
		ST[c]	**2.9971**	**2.7120**	**2.3490**	**0.9931**	**15.0028**
	Analysis	S	**2.2851**	**1.7120**	**1.8140**	**0.9956**	**0.2260**
		T	3.2111	3.3120	2.5929	0.9922	0.2286
		ST	2.3481	1.8120	1.8824	0.9959	0.2627
Lower Fig. 5(a)	Corrupted	\	84.2921	1460.2120	51.3367	0.1523	\
	Synthesis	S	4.2351	5.6120	2.5270	0.9843	6.9092
		T	4.8111	7.9120	2.9363	0.9743	8.5441
		ST	**3.7221**	**4.2120**	**2.2567**	**0.9877**	**15.4823**
	Analysis	S	**2.2081**	**1.6120**	**1.3586**	**0.9951**	**0.2230**
		T	3.9291	5.3120	2.3651	0.9835	0.2241
		ST	2.7951	2.6120	1.6741	0.9921	0.2626

[a] Denotes using only spectral bands.
[b] Denotes using only temporal bands.
[c] Denotes using both the spectral and temporal bands.
[d] Denotes inexistence or non-use; 10^{-3} means the corresponding indicator is multiplied by it, for example, the meaning of 66.9471 is 66.9471×10^{-3}, so does 10^{-5}.

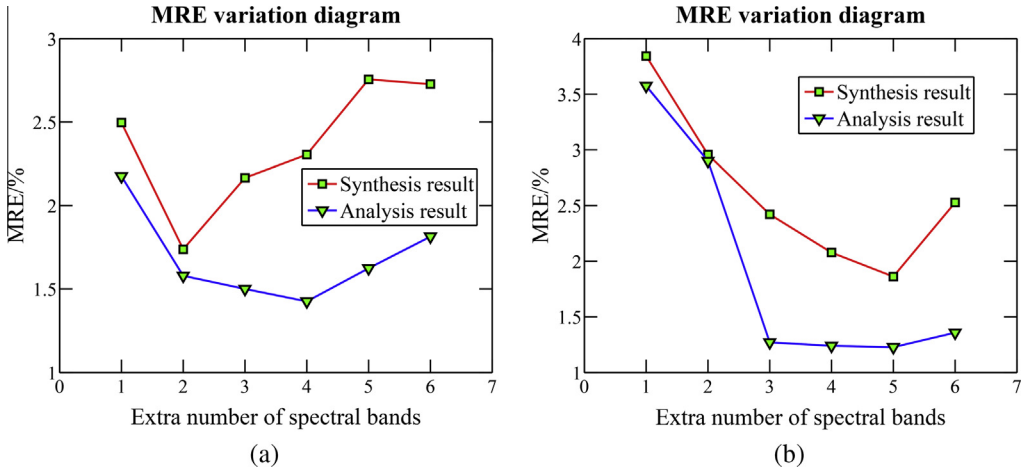

Fig. 7. The MRE variation diagrams of the reconstructions using different extra numbers of spectral bands. (a) For upper Fig. 5(b). (b) For lower Fig. 5(b).

According to their inherent spectral orders, the extra bands were added one by one in the experiments. Note that the corrupted bands were the same as in Fig. 5(b). In order to reveal the changes in the reconstruction results, the MRE variation diagrams of the reconstructions using different numbers of spectral bands (synthesis and analysis models) are shown in Fig. 7. Here, it can be seen from the figures that when using the same number of extra bands, the MRE of the analysis model is lower than that of the synthesis model, which demonstrates that the former reconstructs more accurate result than the latter. As the number of spectral bands increases, the MRE decreases at first, and then increases successively. In other words, using more extra spectral bands does not mean extracting more useful information. This is because when the band setting of the added-in spectral band is very different from the corrupted band, the spectral complementation weakens, and may even become harmful. However, on the condition that the added-in spectral bands can provide valid complementary information, the reconstruction result will become better.

3.2. MI reconstruction with multitemporal images

After the reconstruction capabilities of the synthesis and analysis models were compared with each other from the aspect of extracting spectral complementary information, they were then compared from the other aspect of extracting temporal complementary information. In order to simultaneously compare the results with the multispectral reconstruction results in the previous section, we deliberately chose the same corrupted bands as in the previous section [see Fig. 5(b)]. Since Image A and Image B both have seven spectral channels, for consistency, we chose seven images from different periods in total. To avoid the influence of large areas of a cloudy atmosphere, for the upper Fig. 5(b), we selected other data ordered Nos. 1, 2, 3, 6, 7, and 8 in Table 1 as the experimental data. We then cropped the same region and band of the upper Fig. 5(a) and combined them into Cube A. Similarly, for the lower Fig. 5(b), we additionally selected the data ordered Nos. 1, 2, 3, 5, 7, and 8 in Table 1 and combined their same bands of the lower Fig. 5(b) into Cube B. In other words, Cube A and Cube B were of a size of $300 \times 300 \times 7$.

The visual effect of the reconstruction results using the synthesis and analysis models are compared, as before, in Fig. 8. Note that Fig. 8(b) is the same as Fig. 5(b). As in the experiments using a multispectral image, the visual differences are not obvious. When zooming in on the red box area of Fig. 8, we can see that the analysis model does as well as in the multispectral experiments at both denoising and structure enhancement (see Fig. 5). Additionally, in the reconstruction of the lower Fig. 8(b) with the synthesis model, local anomalies appear, as shown in the green circled areas in the lower Fig. 8(c). After careful checking, we found that one band extracted from the original multitemporal images was

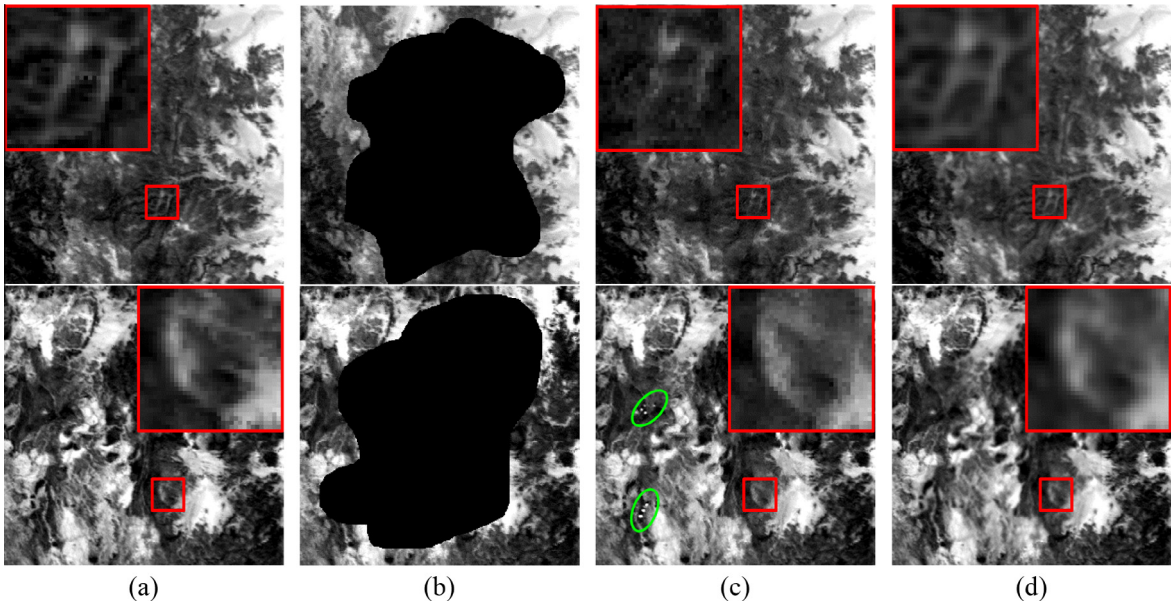

Fig. 8. The reconstruction results of the corrupted Fig. 5(b), based on the synthesis and analysis models, using multitemporal images. The upper row is for Cube A, and the lower row is for Cube B (a) The original image. (b) The corrupted image. (c) Reconstruction of the synthesis model with LTRP. (d) Reconstruction of the analysis model with LTRP.

contaminated by clouds in the same place. Accordingly, the cloud-contaminated pixels were preserved in the reconstruction result. However, this was not what was wanted. In contrast, the results of the analysis model do not show this kind of anomaly [lower Fig. 8(d)]. The results of these experiments indicate that the analysis model avoids the influence of local anomalies more easily than the synthesis model.

The qualitative assessments for the results in Fig. 8 were made with scatter plots between the recovered result and the original data. The scatter plots are shown in Fig. 9. As can be seen, the points in the scatter plots of the analysis model [Fig. 9(b) and (d)] are focused on the diagonal more closely than those of the synthesis model [Fig. 9(a) and (c)]. There are also some obvious outliers in Fig. 9(c) (green[1] circled areas), which amount to anomalies of the green circled areas in the lower Fig. 8(c). As in the multispectral experiments, the analysis model reconstructs more satisfactory results than the synthesis model.

The quantitative evaluations of the reconstructions in Fig. 8 are shown in Table 2 (in this table, the rows with sources labeled T are the objective evaluations for this multitemporal experiment). For all the indicators, the analysis model again outperforms the synthesis model. That is to say, the quantitative assessments are in line with the previous scatter plots and the multispectral experiments. As we know, the temporal complementary information may be damaged by land-cover changes. Consequently, the reconstruction results of the two models are both worse than those using the spectral complementary information (see Table 2 (rows labeled "T")). Additionally, the gap between the synthesis model and analysis model is not as obvious as in Table 2 (rows labeled "T"). The results of these experiments not only demonstrate that the analysis model outperforms than the synthesis model, but they also demonstrate that spectral complementary information is better than temporal complementary information.

For a further comparison of the abilities of the models to extract temporal complementary information, reconstruction of the MI based on different numbers of temporal bands (the same band extracted from multitemporal images) was undertaken. The extra temporal bands were added chronologically. Fig. 10 shows the MRE variation diagrams using different numbers of temporal bands. As in the multispectral experiments, when the same number of temporal bands was used, the MRE of the analysis model was lower than that of the synthesis model. As the number varies, it can be seen that the trends for Fig. 10(a) and (b) are very different. This stems from the fact that the bands from different periods are correlated with the corrupted band differently. When the added-in bands can provide supplementary information, the MRE will decrease; otherwise, it will increase. In the two cubes, their different correlations result in the inconsistent variations in the two subfigures. However, for the same experimental data, the varying results of the synthesis and analysis models are generally accordant.

3.3. MI reconstruction using both a multispectral image and multitemporal images

In the interests of reconstructing the MI, in the previous experiments, the supplementary information was extracted either from the spectral domain or from the temporal domain. In these experiments, we simultaneously extracted complementary information from both the spectral and temporal domains. That is to say, we used the previous multispectral image and the multitemporal images at the same time, according to the synthesis and analysis models. Removing the repetitive corrupted band, we combined Image A and Cube A to form Cube C, and combined Image B and Cube B to form Cube D. As a result, Cube C and Cube D were of a size of $300 \times 300 \times 13$. Moreover, the corrupted bands were kept the same as in Fig. 5(b).

The reconstruction results of the corrupted bands in Cube C and Cube D are shown in Fig. 11. As can be seen in these figures, the reconstruction results are still satisfactory when the spectral and temporal complementary information is simultaneously used. To allow a more intuitive observation, the yellow box areas are zoomed in on. As in the multispectral and multitemporal experiments, the analysis model is good at simultaneous denoising and edge enhancement. Note that for the synthesis model, the

[1] For interpretation of color in Fig. 9, the reader is referred to the web version of this article.

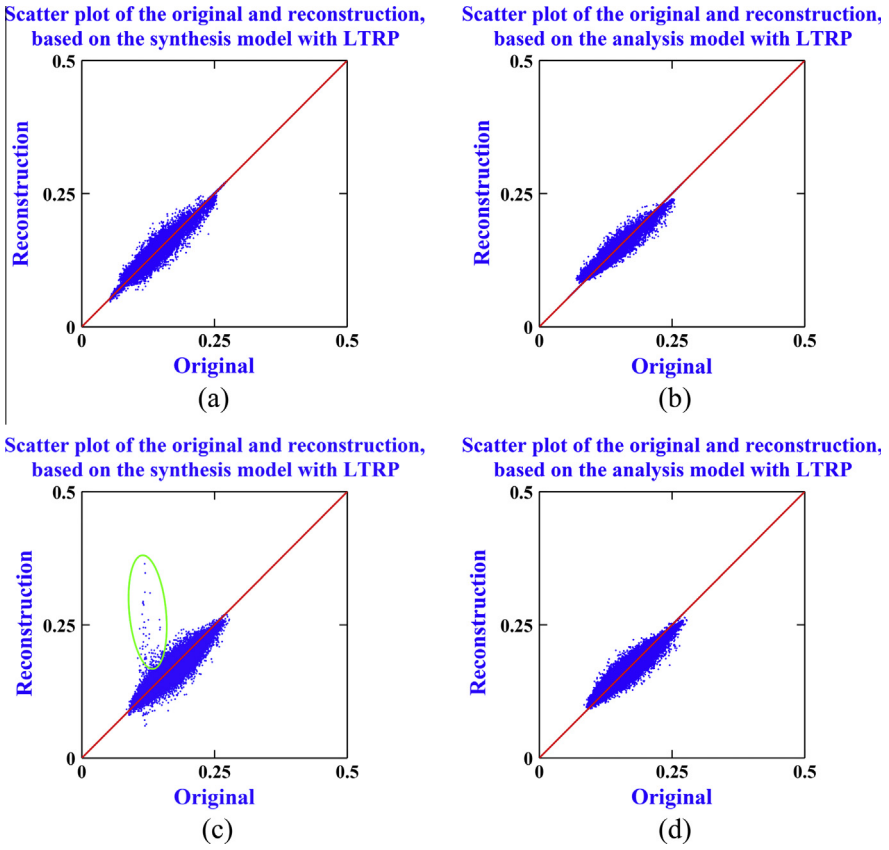

Fig. 9. The scatter plots between the originals and the reconstructions of the synthesis and analysis models in Fig. 8(c)–(d), respectively. (a) For upper Fig. 8(c), synthesis model. (b) For upper Fig. 8(d), analysis model. (c) For lower Fig. 8(c), synthesis model. (d) For lower Fig. 8(d), analysis model.

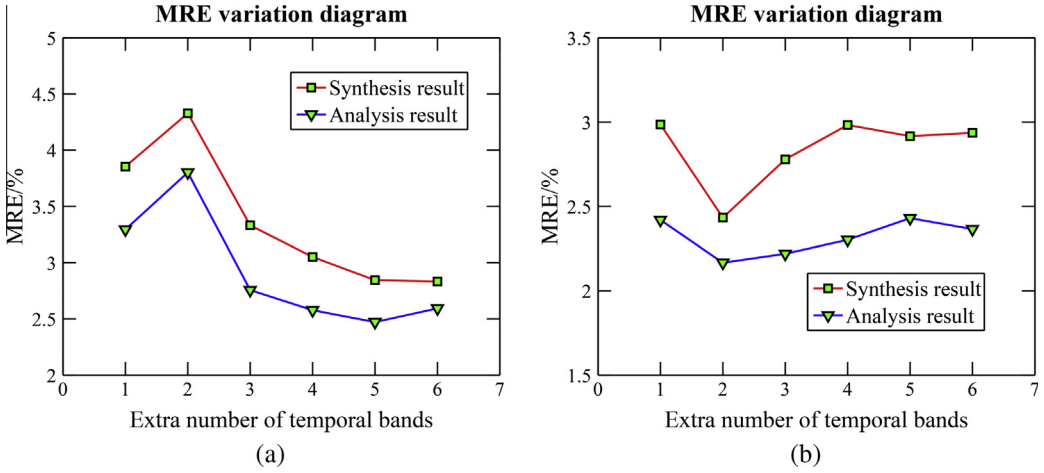

Fig. 10. The MRE variation diagrams of the reconstructions using different extra numbers of temporal bands (the same band extracted from multitemporal images). (a) For upper Fig. 8(b). (b) For lower Fig. 8(b).

anomalies seen in the multitemporal experiments [see lower Fig. 8(c)] no longer appear, which is due to the effective aid of the spectral domain.

The subjective evaluations of the results in Fig. 11 with scatter plots are shown in Fig. 12. The results are again consistent with the previous experiments (Figs. 6 and 9), in that the scatters of the analysis model are more concentrated on the diagonal than those of the synthesis model. These experiments demonstrate that the analysis model is a more promising method. By comparing Figs. 6, 9 and 12, the scatters can be ranked from the most concentrated to the least concentrated: for the analysis model, it is Figs. 6, 12 and 9; for the synthesis model it is Figs. 12, 6 and 9. The reasons for this are explained in the next part.

In order to further reveal which is the best reconstruction approach for extracting information from the spectral domain, from the temporal domain, or from both, the results and the quantitative evaluations for Figs. 5, 8 and 11 are shown in Table 2 (in this table, the rows with sources labeled ST are the objective evaluations for the multispectral and multitemporal experiment). As can be seen in Table 2, the time cost of using both the spectral

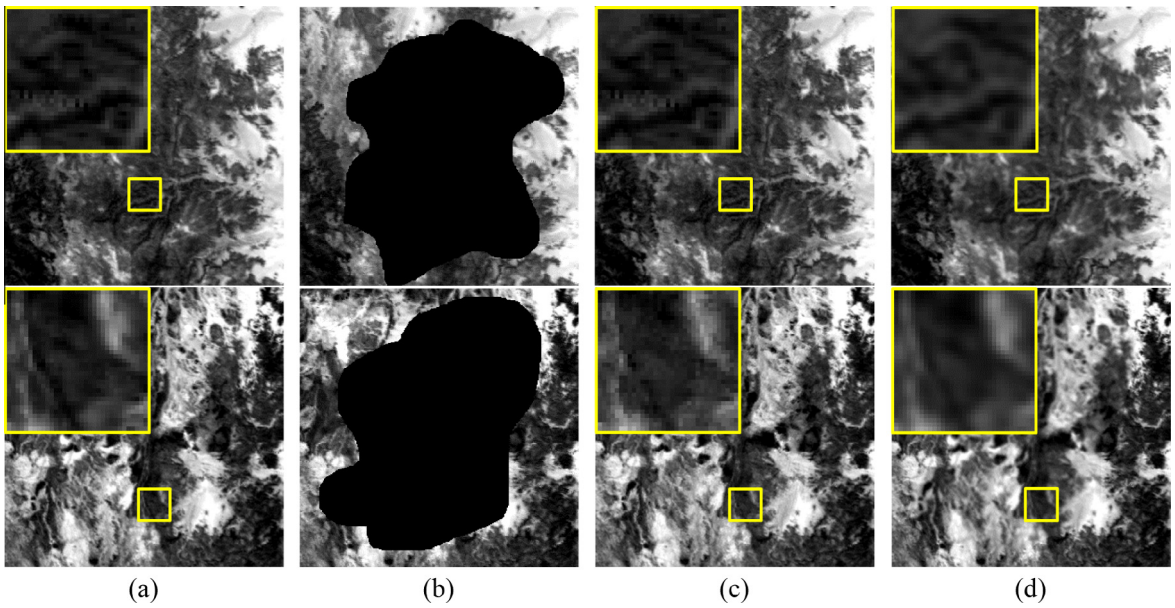

Fig. 11. The reconstruction results of Fig. 5(b), based on the synthesis and analysis models, using the multispectral image and multitemporal images. The upper row is for Cube C, and the lower row is for Cube D. (a) The original image. (b) The corrupted image. (c) Reconstruction of the synthesis model with LTRP. (d) Reconstruction of the analysis model with LTRP.

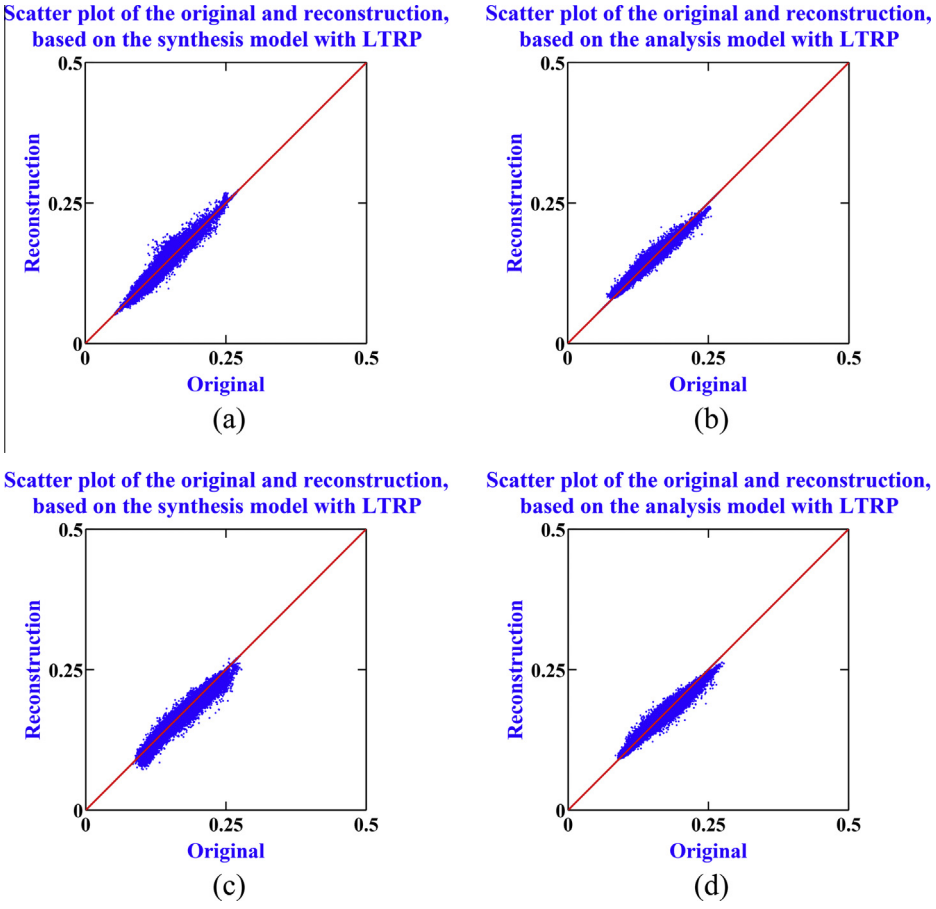

Fig. 12. The scatter plots between the originals and the reconstructions of the synthesis and analysis models in Fig. 11(c)–(d), respectively. (a) For upper Fig. 11(c), synthesis model. (b) For upper Fig. 11(d), analysis model. (c) For lower Fig. 11(c), synthesis model. (d) For lower Fig. 11(d), analysis model.

and temporal information is the highest because the used data cube is the largest. When the complementary information is extracted from the same domain, the analysis model has an advantage over the synthesis model, especially from the aspect of time cost. For the analysis model, the complementary information source ranking from the best to worst is: spectral domain, joint

spectral and temporal domains, and temporal domain. For the synthesis model, the complementary information source ranking from the best to worst is: joint spectral and temporal domains, spectral domain, and temporal domain. As we know, the ground object features and land cover change with time; therefore, extracting information from the temporal domain is the worst approach for both models. However, when adding the temporal information to the spectral information, the reconstructions of the two models are affected differently. As noted by Elad et al. (2007), the analysis model reconstructs the information via forward measurements, so the harmful information has a greater impact on the result. In contrast, the synthesis model reconstructs the information via atom combination, so the harmful information is weakened to some degree. As a result, when combining temporal information with spectral information, the result of the analysis model becomes worse; for the synthesis model, even if the added information is somewhat harmful, it can provide more useful information, and so the result becomes better. On the whole, for the analysis model, extracting information from the spectral domain is the best approach; and for the synthesis model, extracting information from both the spectral and temporal domains is the best approach.

The MRE variation diagrams of the reconstruction results using the synthesis and analysis models with different numbers of spectral/temporal bands are shown in Fig. 13. Note that the horizontal axis has a slightly different meaning here. The "Extra number of spectral/temporal bands" represents the band number in the given domain(s). For example, if the horizontal axis is 4, for "Spectral", it means there are four extra spectral bands being used; for "Temporal", it means there are four extra temporal bands being used; for "Spectral and temporal", it means there are four extra spectral bands and four extra temporal bands being used. As can be seen in Fig. 13, for the two models, as the number varies, the MRE curve using both the spectral and temporal information is the most stable. When the data are sufficient, for the synthesis model, using both the spectral and temporal information gets the best result; for the analysis model, using only the spectral information gets the best result. This is consistent with Table 2.

3.4. MI reconstruction comparisons between the sparse representation methods and others

In Sections 3.1–3.3, we made a comparison with the reconstructions of the synthesis model and analysis model (in the framework of sparse representation). In this section, we focus on comparisons between the sparse representation methods and the other state-of-the-art methods. For the reconstruction of a sequence of RS data, the representative methods include the harmonic analysis of time series (HANTS) method in Roerink et al. (2000) and the SG filter in Chen et al. (2004); thus, we compared them with the sparse representation methods. Although the HANTS method and the SG filter were first applied to the processing of normalized difference vegetation index (NDVI) series data, with a little of modification, they can still be applied to RS images. For consistency, we

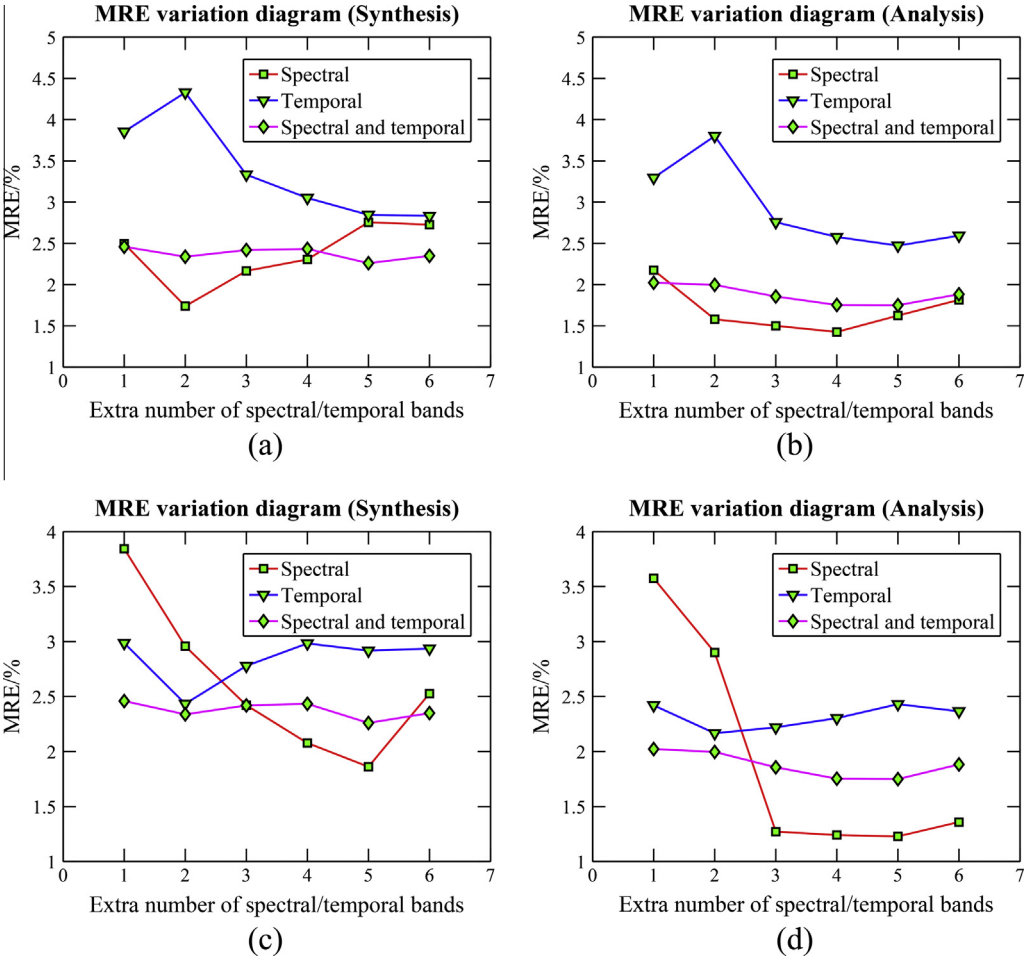

Fig. 13. The MRE variation diagrams of the reconstructions using different extra numbers of single-channel data items. (a) For upper Fig. 5(b), synthesis model. (b) For upper Fig. 5(b), analysis model. (c) For lower Fig. 5(b), synthesis model. (d) For lower Fig. 5(b), analysis model.

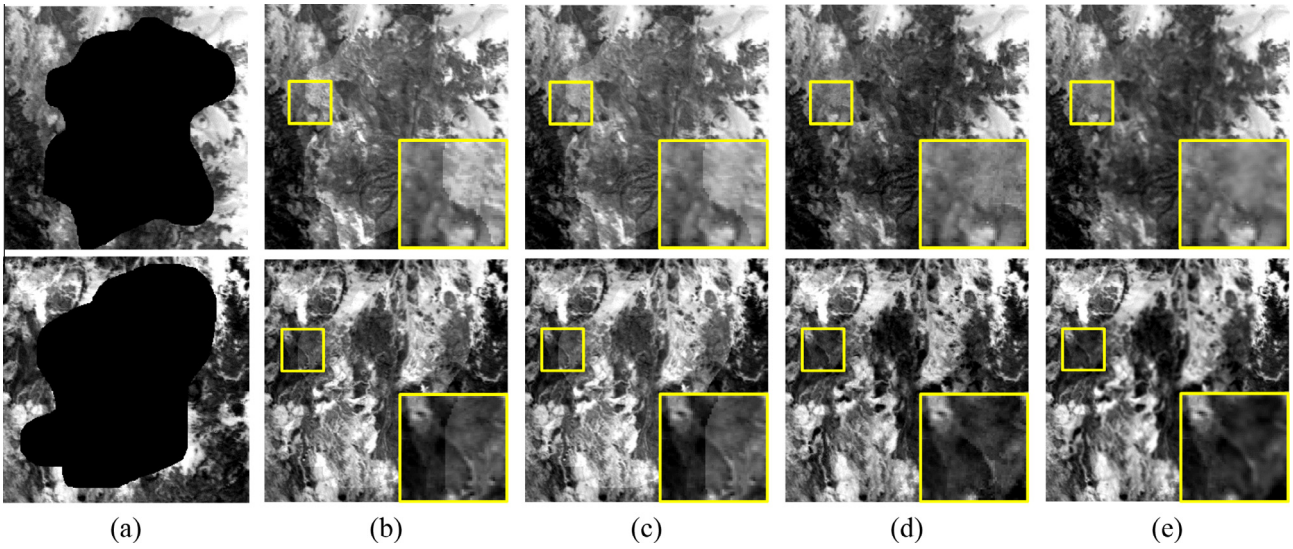

Fig. 14. The reconstruction results of Cube C (upper row) and Cube D (lower row) using different methods. (a) Corrupted images. The results of the following methods: (b) the HANTS method in Roerink et al. (2000); (c) the SG filter in Chen et al. (2004); (d) synthesis model; (e) analysis model.

Table 3
Comparison of the reconstructions in Fig. 14 (sparse methods and other methods).

Data	Methods	MAE/10^{-3}	MSE/10^{-5}	MRE/%	CC
Upper Fig. 14(a)	Corrupted	66.9471	895.6120	52.2133	0.6579
	HANTS	14.2711	42.2120	11.2398	0.9426
	SG	12.3811	30.8120	10.0425	0.9593
	Synthesis	2.9971	2.7120	2.3490	0.9931
	Analysis	**2.3481**	**1.8120**	**1.8824**	**0.9959**
Lower Fig. 14(a)	Corrupted	84.2921	1460.2120	51.3367	0.1523
	HANTS	9.3721	20.3120	6.2673	0.9617
	SG	11.7851	30.9120	7.8679	0.9451
	Synthesis	3.7221	4.2120	2.2567	0.9877
	Analysis	**2.7951**	**2.6120**	**1.6741**	**0.9921**

used the four methods (HANTS, SG filter, synthesis model, analysis model) to reconstruct the corrupted band of Cube C and Cube D, and the visual results are shown in Fig. 14. Here, it can be clearly that the junction of the good area and missing area shows an obvious discontinuity in the results of the HANTS method [Fig. 14(b)] and SG filter [Fig. 14(c)]. However, the results of the synthesis model [Fig. 14(d)] and analysis model [Fig. 14(e)] show a good continuity. This indicates that the sparse representation methods have an advantage over the HANTS method and the SG filter, from the aspect of visual continuity.

The quantitative evaluations of the results in Fig. 14 are shown in Table 3. For MAE, MSE, MRE, and CC, the results for the HANTS method and the SG filter are worse than for the synthesis model and the analysis model. Moreover, the analysis model obtains slightly better results than the synthesis model. In order to further reveal the differences, we show the error statistics curve of the reconstructed area and its corresponding original area for Fig. 14 in Fig. 15, with the four methods, respectively. For both Fig. 15(a) and (b), the errors of the synthesis model and analysis model are mostly concentrated in the neighborhood of zero; however, the errors of the HANTS method and the SG filter are concentrated in the neighborhood of a positive value. In other words, the errors of the HANTS method and the SG filter are higher (positive > negative) than those of the synthesis model and analysis model. In fact, the errors of the HANTS method and the SG filter tend to be positive, which is connected with the basic ideas of the algorithms themselves (for the HANTS method, low value suppression is set; for the SG filter, it makes the data approach the upper envelope). Overall, the sparse representation methods show clear advantages over the HANTS method and the SG filter.

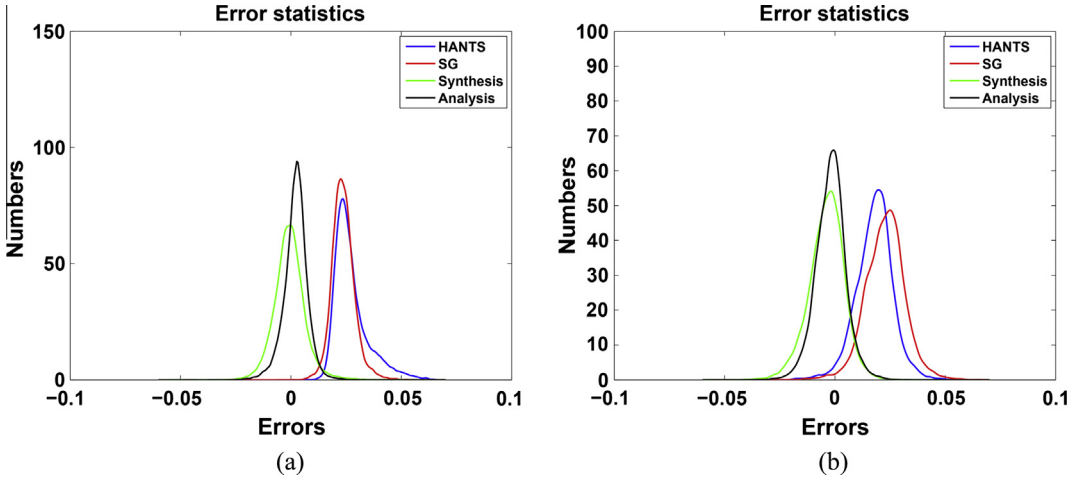

Fig. 15. Error statistics for Fig. 14. (a) For upper Fig. 14. (b) For lower Fig. 14.

4. Conclusions

In the framework of sparse representation, aiming at reconstructing the MI of RS images, this paper has introduced an analysis model, and we made a comparison between the reconstruction abilities of the basic synthesis and analysis models, using spectral complementation only, using temporal complementation only, and using joint spectral and temporal complementation. For reconstructing missing RS information, the analysis model has a clear advantage over the synthesis model by the metrics of MAE, MSE, MRE, CC, and time cost. The experiments indicate that the two sparse models differ in their abilities to extract complementary information from the spectral and temporal domains. For the synthesis model, using joint spectral and temporal complementation is the best way to reconstruct MI when enough images are available. However, for the analysis model, using spectral complementation is the best way. In addition, for the two models, the reconstruction using joint spectral and temporal complementation is more stable than only using one of them. Since it was not easy to find enough data satisfying the requirement of multispectral and multitemporal images over the same geographic area, we did not undertake real data experiments in this study. However, the conclusions will have a guiding significance for the reconstruction of the MI of RS images. In addition, the experiments demonstrate that the sparse representation methods perform better than the current representative methods for reconstructing a sequence of RS images (the HANTS method and the SG filter).

Acknowledgments

This work was supported by the National High Technology Research and Development Program of the P. R. China (863 Program) under Grant No. 2013AA12A301, the National Natural Science Foundation of China (NSFC) under Grant Nos. 41271376 and 41422108, the Wuhan Municipal Science and Technology Bureau under Grant No. 2013072304010825, and the Fundamental Research Funds for the Central Universities of China under Grant No. 2014205020201. The authors would also like to thank the anonymous reviewers.

References

Aharon, M., Elad, M., Bruckstein, A., 2006. K-SVD: an algorithm for designing overcomplete dictionaries for sparse representation. IEEE Trans. Signal Process. 54 (11), 4311–4322.

Bertalmio, M., 2006. Strong-continuation, contrast-invariant inpainting with a third-order optimal PDE. IEEE Trans. Image Process. 15 (7), 1934–1938.

Bertalmio, M., Sapiro, G., Caselles, V., Ballester, C., 2000. Image inpainting. In: The 27th International Conference on Computer Graphics and Interactive Techniques (SIGGRAPH), New Orleans, USA, pp. 417–424.

Chan, T.F., Yip, A.M., Park, F.E., 2005. Simultaneous total variation image inpainting and blind deconvolution. Int. J. Imaging Syst. Technol. 15 (1), 92–102.

Chen, J., Jönsson, P., Tamura, M., Gu, Z., Matsushita, B., Eklundh, L., 2004. A simple method for reconstructing a high-quality NDVI time-series data set based on the Savitzky–Golay filter. Remote Sens. Environ. 91 (3), 332–344.

Cheng, Q., Shen, H., Zhang, L., Li, P., 2014. Inpainting for remotely sensed images with a multichannel nonlocal total variation model. IEEE Trans. Geosci. Remote Sens. 52 (1), 175–187.

Cheng, Q., Shen, H., Zhang, L., Yuan, Q., Zeng, C., 2014. Cloud removal for remotely sensed images by similar pixel replacement guided with a spatio-temporal MRF model. ISPRS J. Photogramm. Remote Sens. 92, 54–68.

Coppersmith, D., Davenport, J.H., 1985. An application of factoring. J. Symb. Comput. 1 (2), 241–243.

Elad, M., 2010. Sparse and Redundant Representations: from Theory to Applications in Signal and Image Processing. Springer, New York, USA.

Elad, M., Aharon, M., 2006. Image denoising via sparse and redundant representations over learned dictionaries. IEEE Trans. Image Process. 15 (12), 3736–3745.

Elad, M., Milanfar, P., Rubinstein, R., 2007. Analysis versus synthesis in signal priors. Inverse Probl. 23 (3), 947–968.

Fadili, M.J., Starck, J.-L., Murtagh, F., 2009. Inpainting and zooming using sparse representations. Comput. J. 52 (1), 64–79.

Gemmeke, J.F., Virtanen, T., Hurmalainen, A., 2011. Exemplar-based sparse representations for noise robust automatic speech recognition. IEEE Trans. Audio Speech Lang. Process. 19 (7), 2067–2080.

Giryes, R., Nam, S., Gribonval, R., Davies, M.E., 2011. Iterative cosparse projection algorithms for the recovery of cosparse vectors. In: The 19th European Signal Processing Conference (EUSIPCO), Barcelona, Spain.

Gladkova, I., Grossberg, M.D., Shahriar, F., Bonev, G., Romanov, P., 2012. Quantitative restoration for MODIS band 6 on Aqua. IEEE Trans. Geosci. Remote Sens. 50 (6), 2409–2416.

Guillemot, C., Le Meur, O., 2014. Image inpainting: overview and recent advances. IEEE Signal Process. Mag. 31 (1), 127–144.

Hawe, S., Kleinsteuber, M., Diepold, K., 2013. Analysis operator learning and its application to image reconstruction. IEEE Trans. Image Process. 22 (6), 2138–2150.

Helmer, E., Ruefenacht, B., 2005. Cloud-free satellite image mosaics with regression trees and histogram matching. Photogramm. Eng. Remote Sens. 71 (9), 1079–1089.

Inglada, J., Garrigues, S., 2010. Land-cover maps from partially cloudy multi-temporal image series: optimal temporal sampling and cloud removal. In: The 30th IEEE International Geoscience and Remote Sensing Symposium (IGARSS), Honolulu, USA, pp. 3070–3073.

Jakubauskas, M.E., Legates, D.R., Kastens, J.H., 2001. Harmonic analysis of time-series AVHRR NDVI data. Photogramm. Eng. Remote Sens. 67 (4), 461–470.

Jianchao, Y., Wright, J., Huang, T.S., Yi, M., 2010. Image super-resolution via sparse representation. IEEE Trans. Image Process. 19 (11), 2861–2873.

Kokaram, A.C., Morris, R.D., Fitzgerald, W.J., Rayner, P.J.W., 1995. Interpolation of missing data in image sequences. IEEE Trans. Image Process. 4 (11), 1509–1519.

Li, X., Shen, H., Zhang, L., Zhang, H., Yuan, Q., 2014. Dead pixel completion of aqua MODIS band 6 using a robust M-estimator multiregression. IEEE Geosci. Remote Sens. Lett. 11 (4), 768–772.

Li, X., Shen, H., Zhang, L., Zhang, H., Yuan, Q., Yang, G., 2014. Recovering quantitative remote sensing products contaminated by thick clouds and shadows using multi-temporal dictionary learning. IEEE Trans. Geosci. Remote Sens. 52 (11), 7086–7098.

Lin, C.-H., Lai, K.-H., Chen, Z.-B., Chen, J.-Y., 2014. Patch-based information reconstruction of cloud-contaminated multitemporal images. IEEE Trans. Geosci. Remote Sens. 52 (1), 163–174.

Lorenzi, L., Melgani, F., Mercier, G., 2013. Missing-area reconstruction in multispectral images under a compressive sensing perspective. IEEE Trans. Geosci. Remote Sens. 51 (7), 3998–4008.

Mairal, J., Elad, M., Sapiro, G., 2008. Sparse representation for color image restoration. IEEE Trans. Image Process. 17 (1), 53–69.

Mallat, S.G., Zhang, Z., 1993. Matching pursuits with time-frequency dictionaries. IEEE Trans. Signal Process. 41 (12), 3397–3415.

Nam, S., Davies, M.E., Elad, M., Gribonval, R., 2013. The cosparse analysis model and algorithms. Appl. Comput. Harmon. Anal. 34 (1), 30–56.

Olshausen, B.A., Field, D.J., 1996. Emergence of simple-cell receptive field properties by learning a sparse code for natural images. Nature 381 (6583), 607–609.

Ophir, B., Elad, M., Bertin, N., Plumbley, M.D., 2011. Sequential minimal eigenvalues – an approach to analysis dictionary learning. In: The 19th European Signal Processing Conference (EUSIPCO), Barcelona, Spain.

Pissanetzky, S., 1984. Sparse Matrix Technology. Academic Press, London, UK.

Rakwatin, P., Takeuchi, W., Yasuoka, Y., 2009. Restoration of Aqua MODIS band 6 using histogram matching and local least squares fitting. IEEE Trans. Geosci. Remote Sens. 47 (2), 613–627.

Ram, I., Elad, M., Cohen, I., 2013. Image processing using smooth ordering of its patches. IEEE Trans. Image Process. 22 (7), 2764–2774.

Rehman, A., Rostami, M., Wang, Z., Brunet, D., Vrscay, E.R., 2012. SSIM-inspired image restoration using sparse representation. EURASIP J. Adv. Signal Process. 2012 (1), 1–12.

Rinaldo, A., 2009. Properties and refinements of the fused lasso. Ann. Stat. 37 (5B), 2922–2952.

Roerink, G.J., Menenti, M., Verhoef, W., 2000. Reconstructing cloudfree NDVI composites using Fourier analysis of time series. Int. J. Remote Sens. 21 (9), 1911–1917.

Rubinstein, R., Peleg, T., Elad, M., 2013. Analysis K-SVD: a dictionary-learning algorithm for the analysis sparse model. IEEE Trans. Signal Process. 61 (3), 661–677.

Shen, H., Zhang, L., 2009. A MAP-based algorithm for destriping and inpainting of remotely sensed images. IEEE Trans. Geosci. Remote Sens. 47 (5), 1492–1502.

Shen, H., Zeng, C., Zhang, L., 2011. Recovering reflectance of AQUA MODIS band 6 based on within-class local fitting. IEEE J. Sel. Top. Appl. Earth Observ. Remote Sens. 4 (1), 185–192.

Shen, H., Li, X., Zhang, L., Tao, D., Zeng, C., 2014. Compressed sensing-based inpainting of Aqua moderate resolution imaging spectroradiometer band 6 using adaptive spectrum-weighted sparse Bayesian dictionary learning. IEEE Trans. Geosci. Remote Sens. 52 (2), 894–906.

Tibshirani, R., Saunders, M., Rosset, S., Zhu, J., Knight, K., 2005. Sparsity and smoothness via the fused lasso. J. R. Stat. Soc.: Series B (Stat. Methodol.) 67 (1), 91–108.

von zur Gathen, J., Kaltofen, E., 1985. Factoring sparse multivariate polynomials. J. Comput. Syst. Sci. 31 (2), 265–287.

Wang, L., Qu, J.J., Xiong, X., Hao, X., Xie, Y., Che, N., 2006. A new method for retrieving band 6 of Aqua MODIS. IEEE Geosci. Remote Sens. Lett. 3 (2), 267–270.

Weisheng, D., Zhang, D., Guangming, S., Xiaolin, W., 2011. Image deblurring and super-resolution by adaptive sparse domain selection and adaptive regularization. IEEE Trans. Image Process. 20 (7), 1838–1857.

Yaghoobi, M., Sangnam, N., Gribonval, R., Davies, M.E., 2012. Noise aware analysis operator learning for approximately cosparse signals. In: IEEE International Conference on Acoustics, Speech and Signal Processing (ICASSP), Kyoto, Japan, pp. 5409–5412.

Yaghoobi, M., Sangnam, N., Gribonval, R., Davies, M.E., 2013. Constrained overcomplete analysis operator learning for cosparse signal modelling. IEEE Trans. Signal Process. 61 (9), 2341–2355.

Yan, H., Chen, L., Tao, J., Su, L., Huang, J., Han, D., Yu, C., 2012. Corrections for OMI SO2 BRD retrievals influenced by row anomalies. Atmos. Meas. Tech. 5 (11), 2635–2646.

Zeng, C., Shen, H., Zhang, L., 2013. Recovering missing pixels for Landsat ETM+ SLC-off imagery using multi-temporal regression analysis and a regularization method. Remote Sens. Environ. 131, 182–194.

Zeng, C., Shen, H., Zhong, M., Zhang, L., Wu, P., 2015. Reconstructing MODIS LST based on multitemporal classification and robust regression. IEEE Geosci. Remote Sens. Lett. 12 (3), 512–516.

Zhang, C., Li, W., Travis, D.J., 2009. Restoration of clouded pixels in multispectral remotely sensed imagery with cokriging. Int. J. Remote Sens. 30 (9), 2173–2195.